Abitare e costruire in un Paese antico. Sicurezza e identità: il progetto di mitigazione sismica della città appenninica come rafforzamento dei suoi caratteri identitari

Real-Time Distance Evaluation System for Wireless Localization

Giovanni Piccinni*, Gianfranco Avitabile*, *Senior Member, IEEE*, Giuseppe Coviello*, Claudio Talarico+

Abstract–The paper describes the FPGA implementation of a novel position evaluation algorithm based on the time difference of arrival (TDOA) principle that combines the characteristics of an Orthogonal Frequency Division Modulation (OFDM) symbol with the properties of the Zadoff-Chu mathematical sequences. The resulting system is highly scalable and its characteristics are easily adaptable to different operating scenarios. The algorithm has been implemented using the Stratix IV-E EP4SGX70HF35C3 FPGA, requiring about 112k bit of memory and less than 44k logic elements of which about 16k are registers. The paper describes the algorithm and its FPGA implementation along with experimental results validating the system performance even in the presence of multipath interferences and showing ~~accuracy~~precision in target position estimation that is better than 2 cm.

***Index Terms*—FPGA, distance estimation, localization, OFDM, positioning, wireless, Zadoff-Chu.**

I. Introduction

In the recent past, wireless localization systems have become extremely popular in several applications and scenarios. Positioning data can be collected to provide location-based services, for example, in automotive applications, they can be used to extract safety information or implement autonomous drive guidance assistance [1].

Due to the different conditions and operating constraints, there is not a general solution to evaluate the target position and, thus, there are several wireless local-positioning systems [2], [3].

Three different principles can be implemented [4] to evaluate the target position. A first solution estimates the position from the measurements of the received signal strength (RSS) [5]. Although these systems are very simple, a fingerprint of the environment is mandatory to improve the accuracy and the precision of the estimates [6]-[7]. A second approach extracts the target position evaluating the angle-of-arrival (AOA) or phase-of-arrival (POA) of the received signal [8]-[9]. In these systems the signal is received by a uniform linear array antenna and the angle information can be extracted employing a software algorithm like MUSIC [10] or one of its variants [11] as ESPRIT [12] or Gold MUSIC [13]. Although these algorithms offer very high accuracy and precision, their implementation is not simple, due to the complex hardware required to process the signal. Research on these topics focuses either on methods to reduce hardware complexity or to introduce novel solutions able to evaluate the angle of arrival with a totally different approach that doesn't require huge computational cost [14], [15], [16], [17]. The last approach exploits the propagation delay of the received signal to extract the target position by ~~triangulation or~~ trilateration methods [18]-[19]. These propagation-time based systems can be further divided into three subsets: time-of-arrival (TOA), roundtrip-time-of-flight (RTOF) and time-difference of arrival (TDOA) [20]-[21].

Among all these possible solutions, uplink-TDOA-based systems have become extremely popular because they require synchronization only between the measuring units but not with the target unit. In fact, in uplink-TDOA-based systems the target is an active device and its position is evaluated by computing the time-difference of arrival of the signals received by at least a couple of measuring units. However, in these systems, the measuring units are able to evaluate only the distance from the target unit, not its absolute position.

The most accurate TDOA methods use Ultra-Wide-Band signals (UWB). Wang et al. [22] propose a radar system that computes the TOA of a static or slow-moving target combining the advantages of interferometry techniques with the properties of the Frequency-Modulated Continuous Wave (FMCW) signals. The system proposed by Wang et al. operates in the 5.8 GHz ISM band and transmits a signal with a bandwidth of 160 MHz, achieving an average accuracy of 1.65 cm. Waldmann et al. [23] combine the FMCW signal with short pulses with a bandwidth of 1 GHz centered around 7.5 GHz to achieve an error of 1.7 cm in the absence of multipath distortions.

Mahfouz et al. [24] introduce a 3D positioning system that implements an 8 GHz carrier signal modulated by a 300ps Gaussian pulse. The experimental results demonstrated in the 3D case a accuracy of 1.53 mm, with an average accuracy of 3.62 mm and a worst-case of 5.6 mm. Lipka et al. [25] propose a novel localization concept whereby the phase of a 24GHz-FMCW signal with a bandwidth of 250 MHz is fed into an extended Kalman filter without any preprocessing. The system locates the target in severe multipath conditions with a 3D accuracy of 1.7 cm. Further TDOA systems based on UWB signals can be found in [26], [27]-[28] and in [29]-[30]-[31].

Although the systems based on the UWB signal offer the highest accuracy and precision (sub-mm accuracy can be obtained), they are much more expensive when compared to other solutions. In fact, digital hardware must process a huge amount of data and the analog front-end must be able to generate pico-seconds pulses. Moreover, the overall system exhibits poor scalability due to the analog front-end designed to manage a UWB signal.

*Department of Electrical and information Engineering, Polytechnic University of Bari, Bari, BA, 70126 Italy e-mail: {giovanni.piccinni,gianfranco.avitabile,giuseppe.coviello}@poliba.it.
+Department of Electrical and Computer Engineering, Gonzaga University, Spokane (WA), USA e-mail: talarico@gonzaga.edu
Manuscript received October , 2019;

This paper describes a novel wireless positioning system based on the uplink-TDOA estimation technique. The sensing signal is a wide-band signal that combines the properties of well-known mathematical sequences with the Orthogonal Frequency Division Multiplexing (OFDM) scheme. The result is a signal that allows for very high accuracy and precision in position estimation. The signal is generated via software and the target positions can be extracted processing the data in digital domain. The system nodes are based on the Software Defined Radio (SDR) architecture, where the analog front-end is in charge of the signal amplification and the up/down frequency conversion. The proposed solution offers a scalable and flexible hardware implementation in a Field Programmable Gate Array (FPGA) that can be modified via software to adjust the signal properties to the channel conditions.

The paper is organized as follows: Section II introduces the mathematical principles of the proposed system with a theoretical description of the overall solution. Section III explains the algorithm outline, while Section IV describes in detail the hardware implementation of the signal processing required to extract the target position. Section V presents the test results performed on the system in an outdoor environment. Finally the conclusion will close this work.

II. Basic Principles

A. Preliminary Considerations

The proposed system exploits a TDOA algorithm to evaluate the 3D position of an active target, using a GPS-like scheme based on four synchronized receivers and a mobile transmitter, designed according to the SDR paradigm. The basic goal of the system is to evaluate the distance between each receiver and the transmitter, using an OFDM symbol composed only by pilot subcarriers, as described in [32]-[33]-[34]. Each subcarrier represents a coefficient of the Frank-Zadoff-Chu (FZC) sequence, generated by the expression below [35]:

$$z(n) = e^{-j\frac{\pi u n^2}{L}} \tag{1}$$

where u is the *root index* and L is the length of the sequence (even value). The equation shows that the coefficients are fixed and the sensing signal samples can be generated off-line in digital form and stored in a suitable look-up table (LUT) and, subsequently, read and used in the computations. The number of subcarriers, the parameters of the sequence and the overall OFDM bandwidth can be varied with a simple software modification, adjusting the system characteristics as a function of the environment and the design specifications. Under this condition, the proposed system can be employed in many different indoor and outdoor localization scenarios by properly scaling the signal properties.

It's important to note from the block diagram of the system in Fig. 1, that the signal is processed entirely in digital form. The analog blocks are in charge only of up/down converting the signal to/from RF/IF frequencies and amplifying it.

The critical aspects of the system are mainly related to the maximum sample rate of the Analog to Digital Converter (ADC) for the receiver chain and the Digital to Analog Converter (DAC) at the transmitter side. Higher sample rates lead to increased precision and accuracy in distance/position estimation but call for higher currents drained from the supply and for the need of processing a huge amount of samples. The relationship between the system parameters and the precision/accuracy will be investigated in the forthcoming sections in order to provide the guidelines for the system design.

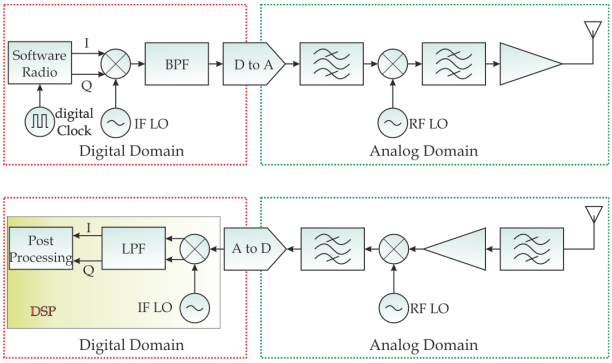

Fig. 1: System Nodes Architecture [36]

B. Algorithm Principles

Let's consider the transmitted OFDM symbol, x(n), composed by N_s subcarriers in which are allocated L coefficients of the FCZ sequence ($N_s \geq L$). The received sequence spectrum, Y(k), can be expressed by:

$$Y(k) = X(k)H(k) + N(k) \tag{2}$$

where $X(k)$ and $H(k)$ are, respectively, the spectrum of the transmitted sequence and the channel transfer function, and $N(k)$ is the additive white Gaussian noise introduced by the channel. If we multiply equation (2) for the conjugate copy of the transmitted sequence spectrum, we obtain:

$$\begin{aligned} &Y(k)X^*(k) = X(k)X^*(k)H(k) + X^*(k)N(k) = \\ &= |X(k)|^2 H(k) + X^*(k)N(k) \end{aligned} \tag{3}$$

The signal and the noise are uncorrelated, thus, the second term in the expression (3) can be neglected. As mentioned, the FCZ sequences have a constant amplitude ($|X(k)|^2 = 1$) and the first term is equal to the channel transfer function $H(k)$. Obviously, the channel impulse response can be extracted applying the Inverse Fast Fourier Transform (IFFT) on equation (3).

Under this assumption, we consider the time delay, δ_i, introduced by the path interconnecting the transmitter and the i-th receiver and ϵ_i the associate carrier frequency offset. Assuming a time-discrete representation for the signals, δ_i can be expressed as a function of the index of the sample in the sequence. The Additive White Noise Gaussian (AWGN) channel model can be expressed as follows:

$$h(n) = \sum_{k=0}^{N-1} \alpha_i e^{-j\frac{2\pi(n+\delta_i-\delta_T)(k+\epsilon_i-\epsilon_T)}{N}} \tag{4}$$

where N is the IFFT length and α_i is the geometric attenuation associated with the i-th line-of-sight. The unwanted terms δ_T and ϵ_T represent, respectively, the initial time-shift and the

initial carrier offset shift, due to the absence of synchronization between the transmitter and the receivers. This result demonstrates another significant property of the FZC sequences, that is, the magnitude of the time cross-correlation function is non-zero only at the instant that corresponds to the time-delay between the signal involved in the computation (Fig. 2).

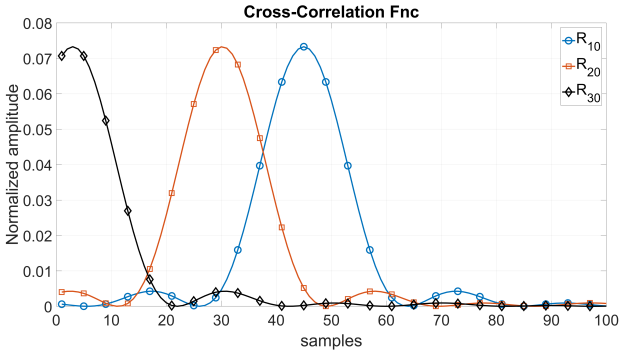

Fig. 2: Examples of the cross-correlation function for different distances: the peak moves farther to the right as a function of the increased delay. The delay is measured by means of the sample number (x-axis) times the sampling time

The i-th distance can be estimated evaluating this time-delay, δ_i, from the cross-correlation function in the time-domain and, in the frequency domain, from the carrier frequency offset, ϵ_i, expressed by the phase of equation (3). Unfortunately, the unwanted terms δ_T and ϵ_T are present in equation (4), representing, respectively, the initial time-shift and the initial carrier offset shift, due to the absence of synchronization between the transmitter and the receivers. The estimate of these terms is necesssary in order to evaluate the desired parameters, δ_i and ϵ_i. In the TDOA approach, the evaluation of these terms is obtained by synchronizing the receivers and performing differential measurements, in which one of the receivers is taken as a reference for the whole set of receivers. Let's consider Rx_0 as the reference receiver and $y_0(k)$ the received sequence. To estimate the time difference of arrival, the signals received by the other devices are multiplied by the conjugate spectrum of signal $y_0(k)$. In this case, equation (4) assumes the form:

$$h(n) = \sum_{k=0}^{N-1} \alpha_0 \alpha_i e^{-j\frac{2\pi(n+\delta_0-\delta_i)(k+\epsilon_0-\epsilon_i)}{N}} \tag{5}$$

where α_0, δ_0 and ϵ_0 are the geometric attenuation, the time-delay and the carrier frequency offset of the reference receiver, respectively, while α_i, δ_i and ϵ_i are the geometric attenuation, the time-delay and the carrier frequency offset of the i-th receiver, respectively ($i = 1, 2, \ldots, M$ total number of receivers). Other terms that represent the time and the frequency shift between the transmitter and each receiver elide because they are equal for any possible couple of terms considered in equation (5).

Once estimated the difference $\Delta\delta_i = \delta_0 - \delta_1$ and $\Delta\epsilon_i = \epsilon_0 - \epsilon_i$, these two pieces of information are combined to obtain the difference between the two distances, d_{i0}. As mentioned, the value of $\Delta\delta_i$ is extracted from the cross-correlation function in (5) and its estimated value depends on the sampling time of the ADC. In fact, the minimum detectable differential distance corresponds to the condition when the auto-correlation peaks are distinct [36]. This spatial condition corresponds in the time domain, to the minimum time step, that is, the sampling time. Hence, the term $\Delta\delta_i$ represents only a first estimate of the distance difference between the received signals and it should be refined with a further step, in which the phase of (3) is evaluated. The example reported in Fig. 3 points out that the phase varies linearly as a function of the frequency, due to the linear relationship between the subcarriers. In fact, to guarantee the orthogonality of the resulting signal, the j-th subcarrier frequency is equal to $j\Delta f = jBw/Ns$, where Bw is the signal bandwidth. The slope α of the straight lines in Fig. 3 depends on the time-delay between the received signals:

$$\alpha = \Delta\delta_r \Delta f \tag{6}$$

where $\Delta\delta_r$ is the residual time-delay that is not computed by the value extracted from the cross-correlation function. On the contrary, the offset of the straight line represents the carrier frequency offset, $\Delta\epsilon_i$, between the carriers of the received signals and it depends only on the system wavelength, λ.

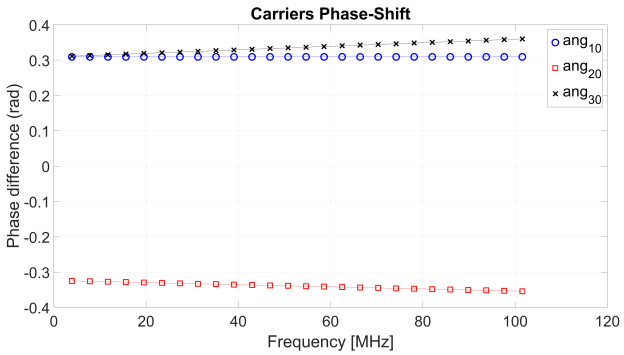

Fig. 3: Example of the carrier phase shift evaluation. The value of ang_{i0} gives the phase difference between the incoming signals at the $i-th$ and the reference receiver, in radians, as a function of the sub-carrier frequency.

Once the coarse delay, $\Delta\delta_i$, the fine delay increment, $\Delta\delta_r$, and the offset of the straight line, $\Delta\epsilon_i$, have been evaluated, these terms are combined to compute the distance difference, d_{i0}:

$$d_{i0} = (\Delta\delta_i + \Delta\delta_r)\, v_p + \Delta\epsilon_r \lambda \tag{7}$$

where v_p is the signal propagation velocity ($v_p \simeq 3 \cdot 10^8 m/s$ in air).

Finally, the distance differences are transmitted to a central unit to extract the target position, (x_t, y_t, z_t), solving the equation system that describes the geometric model of the

localization system [18]:

$$\begin{cases} (x_t - x_{R_0})^2 + (y_t - y_{R_0})^2 + (z_t - z_{R_0})^2 - (d + d_0)^2 = 0 \\ (x_t - x_{R_1})^2 + (y_t - y_{R_1})^2 + (z_t - z_{R_1})^2 - (d + d_1)^2 = 0 \\ (x_t - x_{R_2})^2 + (y_t - y_{R_2})^2 + (z_t - z_{R_2})^2 - (d + d_2)^2 = 0 \\ (x_t - x_{R_3})^2 + (y_t - y_{R_3})^2 + (z_t - z_{R_3})^2 - (d + d_3)^2 = 0 \\ d_1 - d_0 - d_{10} = 0 \\ d_2 - d_0 - d_{20} = 0 \\ d_3 - d_0 - d_{30} = 0 \end{cases} \tag{8}$$

where d_i are the distances between the receivers and the transmitter, d_ij are the measured distance differences, and $(x_{R_i}, y_{R_i}, z_{R_i})$ are the coordinates of the i-th receiver, being, usually, $(x_{R_0}, y_{R_0}, z_{R_0})$ set as the origin of the Cartesian axes. The system described by equation (8) highlights how the precision and the accuracy in the target position estimation depends even on the receivers' coordinates. If the coordinates of the receivers are noisy, the accuracy and the system precision will be degraded as well. However, this problem is common to any localizing system based on the TOA and the TDOA algorithms and its effects on the system precision and accuracy have been investigated [4]. Further details about the algorithm can be found in [37] where the pseudo-code of the entire method was presented.

III. Algorithm Outlines

The key advantage of the proposed solution lays its high scalability. The proposed system is not designed for a specific application and it can be used to extract the target position in both indoor and outdoor environments, with different degrees of ~~accuracy and~~ precision. In fact, the signal parameters can be adjusted as a function of the desired ~~accuracy~~precision and the target application. Due to the OFDM modulation scheme used to arrange the fixed FZC pilot subcarriers, the relationship between the signal parameters can be expressed as:

$$Bw = \frac{Ns}{N} \times f_{clk} \tag{9}$$

where Bw is the bandwidth, N is the FFT size, N_s is the number of subcarriers, and f_{clk} is the sample rate. Hence, taking a fixed FFT size for the digital signal processing, the remaining parameters can be properly adjusted to vary the signal bandwidth and/or the number of subcarriers, thus achieving a different degree of precision ~~and accuracy~~. This task can be easily performed via software, by storing in the transmitter separate LUTs with different versions of the signal. The user can select the desired version addressing the FPGA at the correct memory location. The transmitting sample rate and the ADC clock must be adjusted using PLLs with embedded clock dividers to guarantee the absence of aliasing.

As explained in [36], the precision ~~and the accuracy~~ of the system is a function of the signal parameters. Fig. 4 shows the variation of the system ~~accuracy~~precision as a function of the signal bandwidth for different signal to noise ratios (SNR) at the input of the receiving chain. ~~To obtain these curves, a signal composed by 64 subcarriers was considered in the model of the system~~These curves were extracted by modeling the system using a signal composed of 64 subcarriers. The signal was sampled with a fixed sampling frequency of 1 GHz and an additive white gaussian noise (AWGN) channel was considered. The resulting values were compared to the Cramer-Rao lower band (CRLB) that furnishes the theoretical ~~accuracy~~precision limit for the system [38]. As depicted in Fig. 4, the ~~accuracy~~precision has a trend that is a linear function (in logarithmic scale) of the SNR. Basically, as the SNR increases the system ~~accuracy~~precision increases as well. At higher SNRs the system ~~accuracy~~precision converges to the CRLB limit. It's important to note that the signal ~~accuracy~~precision at 5dB of SNR is better than 10 cm using 64 subcarriers with a bandwidth of only 20MHz. Similar considerations can

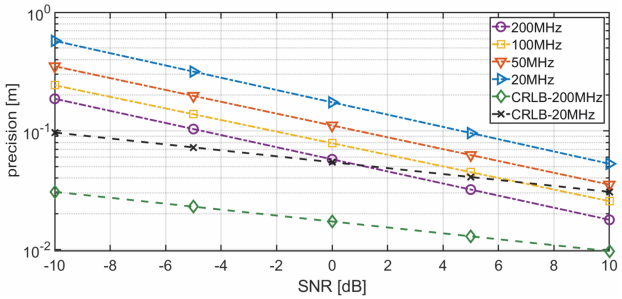

Fig. 4: System ~~accuracy~~precision as a function of the SNR [36]

be made when the number of subcarriers changes. In Fig. 5 is shown the system ~~accuracy~~precision as a function of the number of subcarriers. In this case, the signal bandwidth was fixed to 100 MHz, while the sampling frequency and the channel model are the same reported in the previous paragraph. The system ~~accuracy~~precision is again a linear function (in logarithmic scale) of the SNR. For higher SNR, the system ~~accuracy~~precision converges to the limit defined by the CRLB. The curves highlight that the theoretical ~~accuracy~~precision

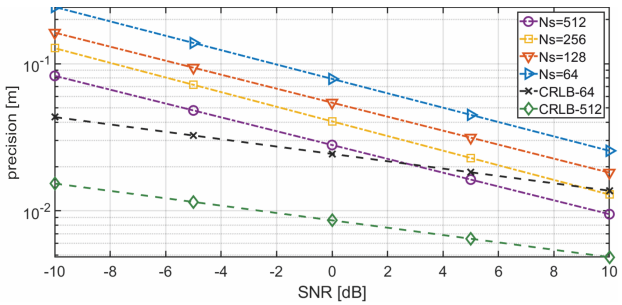

Fig. 5: System ~~accuracy~~precision as a function of the number of subcarriers [36]

is of the order of 4.5 cm with 5dB of SNR, considering 64 subcarriers. On the contrary, with the same SNR and 256 subcarriers, the ~~accuracy~~precision more than halves with respect to the previous case (2 cm).

Fig. 6 reports the system ~~accuracy~~precision as a function of the sampling rate. If the sampling rate increases, the ~~accuracy~~precision increases as well. The resulting values were extracted considering an FFT size of 256 points and adjusting

the subcarriers' length and the bandwidth according to equation (9).

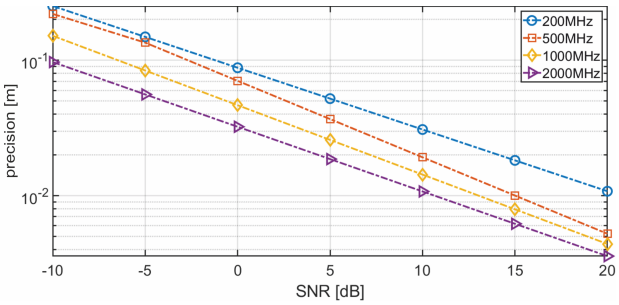

Fig. 6: System ~~accuracy~~precision as function of the sampling rate [36]

Even though the increment of the sampling rate allows to extract the target positions with higher ~~accuracy~~precision, the resulting system drains more DC power and calls for expensive FPGAs that require higher clock frequency. These are obvious consequences of the parameters selection in equation (9) and depend on the target application and the desired system ~~accuracy~~precision. The curves previously discussed can be used as an aid to select the proper system parameters.

Further advantages of the proposed method can be obtained from the generation of the sensing signal. This one can be generated in the digital domain once and forever and the associated samples can be pre-loaded in memory to reduce the computation of the cross-correlation function.

Finally, due to the orthogonal property of the Zadoff-Chu sequence as a function of the root index, more than one transmitter can be localized at the same time without introducing any interference. In this case, the position of a proper target is extracted using the reference copy of the sensing signal with the specific root index.

IV. Real-Time Algorithm Implementation

The algorithm described in section II-B has been implemented in an FPGA to test its real-time performances. The received signal is acquired by an ADC with a maximum sampling frequency of 250 MHz and 12-bits resolution. The resulting samples are represented in fixed point arithmetic.

Fig. 7 shows the block diagram of the hardware implementation of the system. Its digital part is divided into four main blocks:

- spectra-estimator
- time-estimator
- frequency-estimator
- distance aggregator

The *spectra estimator* performs three fundamental functions. The first function is to take the IF signal, acquired by the ADC, and down-convert it to baseband frequency through a digital I/Q demodulator. The use of a digital I/Q demodulator gives the main advantage of not introducing any mismatch between the amplitude, frequency, and phase between the I and Q channels. Once the IF signal is converted into baseband samples, the second function of the *spectra*

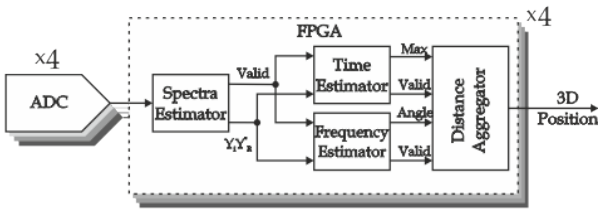

Fig. 7: System Block Diagram

estimator is to compute their *Fast Fourier Transform* (FFT). Note that baseband signal samples are complex numbers and therefore two FFT-cores are needed one for the real part and one for the imaginary part. The FFT-cores have a size of 256-points and 12-bits of resolution. The parameters of the FFT are imposed by the number of subcarriers composing the OFDM symbol and the bandwidth of the transmitted signal. To reduce the system latency, the FFT-cores accept the input samples in natural order and output the resulting samples in digit-reverse order [39]. The FFT-cores are implemented using a fully pipelined radix-2^2 single delay feedback architecture. In this case, the FFT blocks introduce a time-latency of N=256 clock cycles, essentially due to the buffers filling process. Once the FFT computation is completed the FFT-cores provide a valid flag, that is used to enable the last function of the *spectra estimator*, that is, a sample by sample multiplication of the spectra. The result of each FFT-core is multiplied, sample by sample, by the conjugate copy of the transmitted signal spectrum, whose samples are stored in advance (see Fig. 8) in a LUT. The multiplication is then fed in parallel to both the *time-estimator* and the *frequency-estimator*.

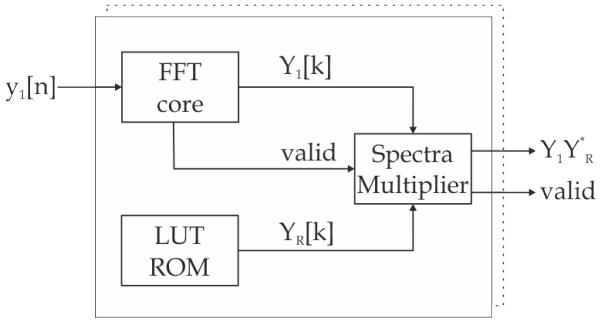

Fig. 8: Diagram illustrating the spectra product in the receiver

The *time-estimator* and the *frequency-estimator* start operating only when the spectra multiplication operation is completed and does issue them a valid flag. The *time-estimator* performs a coarse estimate of the distance between the transmitter and the receiver by evaluating the cross-correlation between the signal received and a copy of the transmitted signal. To compute the cross-correlation function between the two sequences, the proposed algorithm perform the IFFT of the spectrum provided by the spectra multiplication block

only after having introduced a zero padding that makes the sequences 1024 points long. The zero-padding operation increases the size of the IFFT but results in a higher resolution in terms of the time domain points [40]. This operation allows to obtain a smoother cross-correlation function and therefore provides a less granular estimates of its peak's amplitude. In practice, to reduce latency, and chip-area, it is possible to exploit symmetry and perform the 1024-points IFFT operation by using four 128-points IFFT-cores [39]. Fig. 9 shows an accurate diagram of how the main blocks of the distance estimation algorithm have been implemented in the FPGA. The reference signal, $y_R[n]$, is read from an external LUT containing its time-domain samples. This design choice has been made to use this basic block as stand-alone unit, in the simplified 1D distance measurement scenario. In fact, in this case we need only two receivers whose outputs could be directly cross-correlated in order to extract the TDOA between the two received signals.

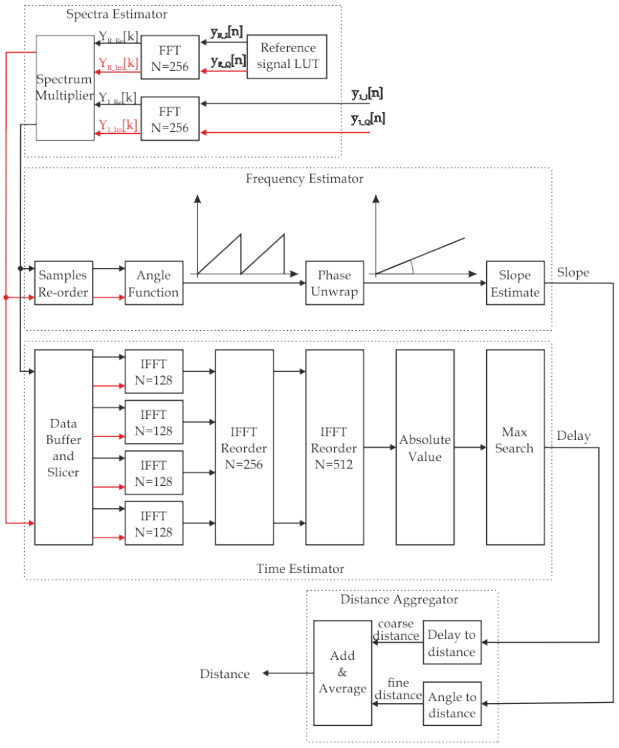

Fig. 9: Diagram illustrating the FPGA implementation of the distance estimation algorithm. Red lines evidences the imaginary parts of the spectra and the Q component in the time-domain

The *frequency-estimator* performs a fine-grained estimate of the distance between the transmitter and the receiver by evaluating the phase-shift of the sub-carriers between the received signal and the reference signal, according to the theory discussed in Section II and using equation (6) to evaluate the slope of the straight line representing the phase-shift as a function of the carrier frequency. To compute the phase-shift of the subcarriers correctly, the samples need to be re-ordered with respect to the order in which they are stored after the spectrum multiplication. The slope is expressed by the following formula:

$$slope = \arctan\left(\frac{ImY_1[k]\, Y_R^*[k]}{ReY_1[k]\, Y_R^*[k]}\right) \tag{10}$$

Due to the presence of the time-delay introduced by the channel, and the periodicity of the tangent function, when the estimated subcarriers' phase-shift values exceed the range between $-\pi/2$ and $+\pi/2$, the phase is wrapped. Therefore, to estimate the sub-carriers phase shifts correctly, the values must be un-wrapped along a continuous varying straight line. This task is performed by the unwrap block.

Finally, the *distance aggregator* combines the coarse distance estimates computed in the time domain, with the fine-grained estimates computed in the frequency domain, and averages the results over a number of acquisition cycles of the OFDM-FZC signal. The algorithm provides a valid value every N clock cycles, so if the FPGA, for example, operates at a 250 MHz clock frequency, it produces a valid sample with a frequency of $250MHz/256 = 975KHz$.

A. FPGA test implementation

The physical implementation of the algorithm has been mapped into a Stratix IV-E EP4SGX70HF35C3 FPGA. The FPGA coding was done in VHDL and is toroughly described in [41]. Despite the algorithm requires two 256-points FFT cores and four 128-points IFFT cores, its implementation has been optimized into about 44k logic elements (60%of the FPGA capability), 112k memory bits (2% of the FPGA capability) and 134 embedded DSP elements (34% of the FPGA capability). Table I summarizes the exact overall FPGA's resources allocation, and Fig. 10 illustrates what percentage of resources are allocated to each block in the system including the FFT/IFFT cores. The FPGA used to implement the system is built on an optimized 40-nm low power CMOS process with 0.9 V supply voltage. The average power consumption of the system is only 381.75 mW. The percentage power consumption for each block of the system, including the FFT/IFFT cores, is reported in Fig. 11, while Fig. 12 depicts the layout of the system.

TABLE I: FPGA Resources Utilization.

Register	15697
Combinational Logic	27799
Total Logic Elements	43496/72600 (60%)
Memory Bits	111136/6617088 (2%)
Embedded Multiplier Elements	130/384 (34%)

V. Experimental Results

To validate the proposed architecture and to demonstrate its scalability, the complete system has been implemented using standard Texas Instruments' hardware. The transmitter is composed of the FPGA evaluation platform TSW1400EVM and the DAC evaluation board DAC3482EVM which has on-board a dual-channel, 16-bit, 1.25-GSPS DAC. Each receiver is composed of the FPGA evaluation platform TSW1400EVM and the ADC evaluation board ADS4249EVM, which has on-board a dual-channel, 14-bit, 250-MSPS ADC. The boards

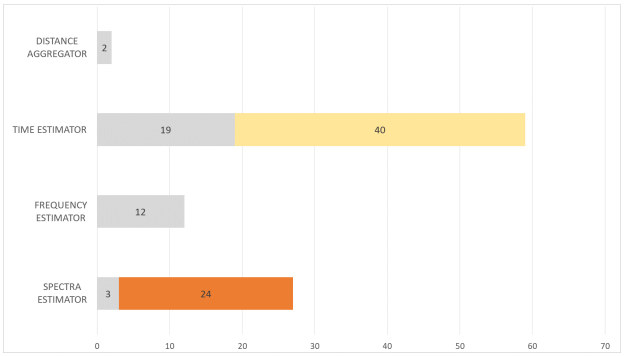

Fig. 10: Resource allocation in percentage

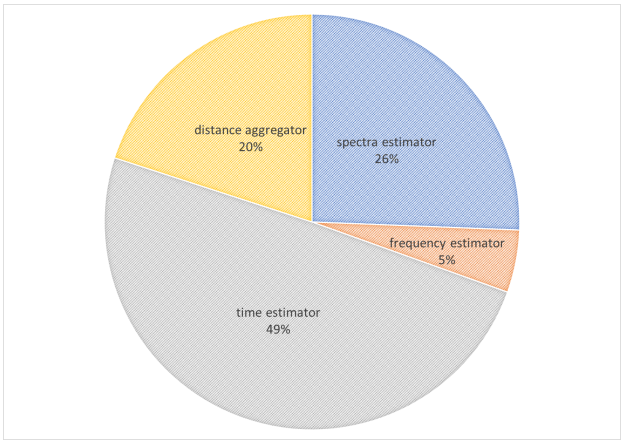

Fig. 11: Dissipated power in percentage

need an external clock provided by a clock cleaner and fed to the FPGAs through the LVDS interface.

The transmitting and receiving front-end have been expressly designed, using a 2x2 patch array antenna. Fig. 13 depicts the receiving unit. The downconverter board integrates an Automatic Gain Control (AGC), ensuring optimum use of the ADC dynamic range.

The experimental validation was carried out in an outdoor environment using a single transmitter in line-of-sight with four receivers, placed in *a priori* known positions. Fig.14 depicts a plan view sketch of the positions of the receivers (green boxes) and the transmitter (red box) in its starting and final position in a Cartesian reference system. The transmitter initial position defines the origin of the system. The transmitter uses a 40MHz signal bandwidth. The receivers share the same ADC clock for synchronization. The distance between the transmitter and the receivers is about 10 m and the transmitter moves on a 2 m long rail, in 20 cm steps, in eleven successive positions. One of the four receivers is used as a reference for the differential distance measurements.

The measurement accuracy is a significant system parameter as well as its repeatability and, as stated before, its scalability. Two different test benches have been implemented by changing the clock frequency of the clock cleaner at the input of the ADC board and the copy of the transmitted signal stored in the LUT. The first test bench uses a 100MHz clock and the second one uses a 250MHz clock. For each transmitter position

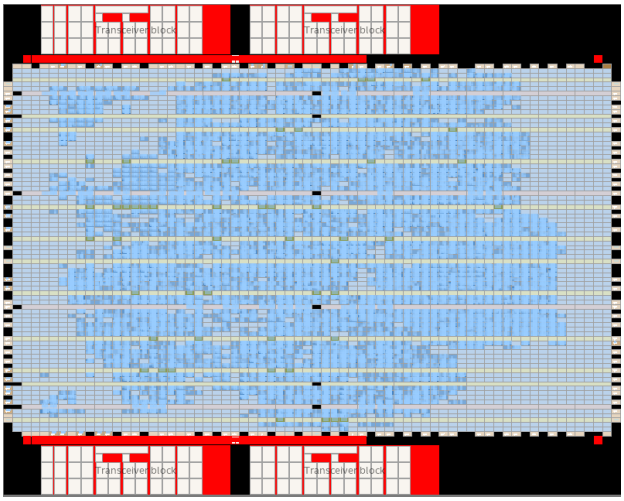

Fig. 12: FPGA layout

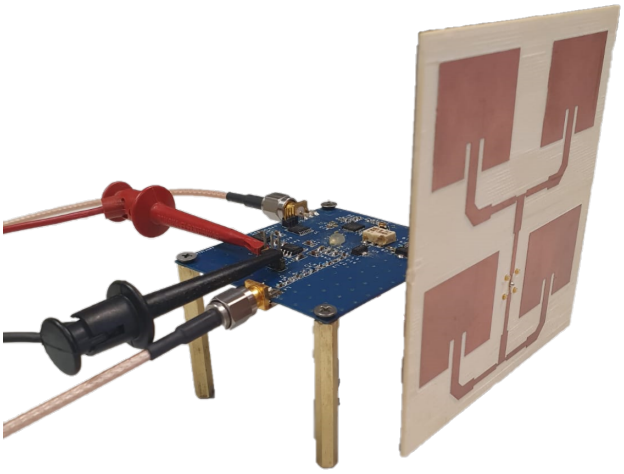

Fig. 13: Upconverter with the 2x2 patch array antenna

each receiver performs 10 distance measurements and stores the values in local memory.

A class 2 laser distance measurer with a 0.1mm resolution, ±2mm accuracy, and ±0.5mm repeatability is used as a term of comparison for distance evaluations. As shown in Fig.15, each patch array antenna integrates an *ad hoc* fabricated mechanical structure to help the laser pointing and measuring. For each transmitter position, the four distances measured with the laser are memorized and compared with the system measurements.

A. 100 MHz ADC sampling frequency

In the first scenario, the ADC clock is 100MHz. In Fig. 16 are shown the comparisons with a single differential measure made by our system and a single differential measure made by the laser system for each couple of receivers RX2-RX1, RX3-RX1, RX4-RX1, where RX1 is used as the reference.

Fig. 17 shows the measurement error for each couple of receivers while Fig. 18 shows the percentage difference distance measurement error.

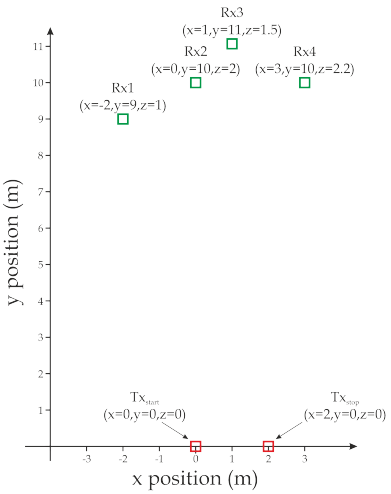

Fig. 14: Receivers (green boxes) and transmitter (red boxes) plan view displacement representation

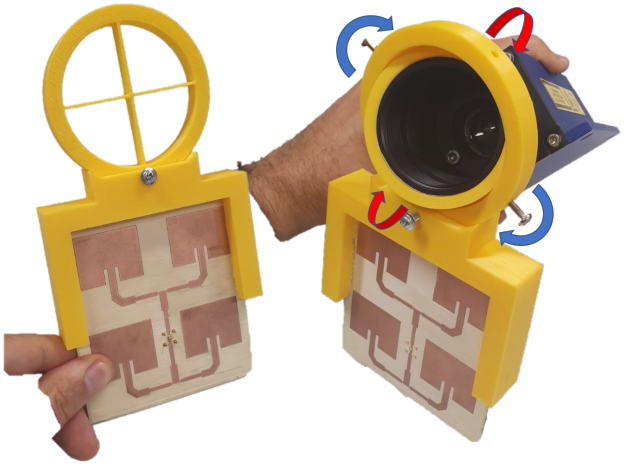

Fig. 15: Laser pointing structure

Fig. 19 exemplifies the system repeatability for the couple of receivers RX2-RX1, reporting the standard deviation for a set of 10 measures and for a 1 m TX shift.

The worst case maximum error reported is of the order of 8 cm with a precision of 0.7 cm. It is important to underline that the error value is mostly due to the ADC sampling frequency used, while the precision is independent by the used ADC sampling frequency.

B. 250 MHz ADC sampling frequency

In the second scenario, the ADC clock is increased up to 250MHz, while nothing else was changed except for the LUT. The same measurements previously described have been performed to demonstrate the scalability of the architecture. Fig. 21 shows the comparisons with a single differential measure made by our system and a single differential measure made by the laser system for each couple of receivers RX2-RX1, RX3-RX1, RX4-RX1, where RX1 is taken as the reference.

Fig. 22 shows the measurement error for each couple of receivers, while Fig. 23 reports the difference distance measurement error in percentage.

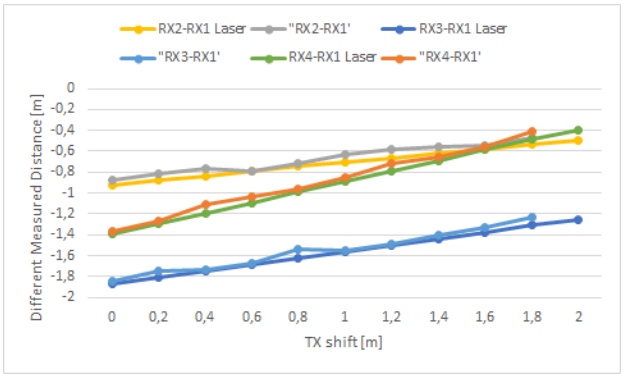

Fig. 16: Difference measured distance

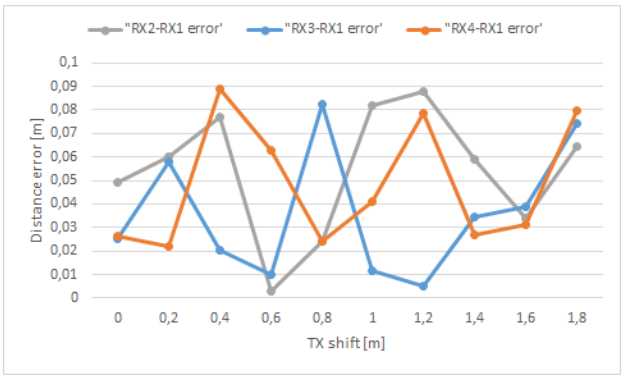

Fig. 17: Difference distance measurement error

The repeatability for one single couple of receivers RX2-RX1 is shown in Fig. 24, reporting the standard deviation for a set of 10 measures and for a 1 m transmitter displacement.

In this scenario the maximum error reported is about 2 cm. The precision is similar as in the previous scenario and it is of the order of 0.7 cm.

Table II shows the measured values for a 10 dB SNR and a 100 and 250 MHz sampling rate. The table reports for each sampling rate the distance evaluation obtained, respectively, by the RX2-RX1, RX2-RX3, and RX3-RX1 couples. The same table lists the maximum and minimum errors along with the mean values and standard deviations. The last column gives the reference values provided by the CRLB.

Table III compares the proposed system with the most accurate and precise results in the literature. It is worth to point out that although our approach is slightly less accurate, it uses a bandwidth significantly smaller than the other methods, all based on the UWB approach.

VI. Conclusions

The paper describes the FPGA implementation of a novel distance measuring technique. The method uses an OFDM signal coded using FZC sequences and extracts the distance between the active target and each measuring unit with a TDOA algorithm. The precision and the accuracy achieved by the system even with small bandwidths (in the order of tens of MHz) are comparable with significally more complex methods that use UWB signals. The key advantage of the proposed

TABLE II: Statistical analisys of the measurements and comparison with CRLB

	Meas. SNR=10dB (cm)										Max (cm)	Min (cm)	AVG (cm)	STD (cm)	CRLB (cm)
Fs=100MHz	5	6	7.8	0.2	2.5	8	9	6	3	6.5	9	0.2	5.4	2.8	1.5
	2.5	6	2	1	8	1	0.5	3.2	4	7.6	8	0.5	3.6	2.7	1.5
	2.8	2	9	6.1	2.2	4	8	2.7	3	8	9	2	4.8	2.7	1.5
Fs=250MHz	1.8	0.2	0.1	1.4	1.8	1	1.9	1.6	1	1.9	1.9	0.1	1.3	0.7	0.3
	0.2	1.2	0.7	0.5	1.5	0.9	0.5	0.2	0.5	0.1	1.5	0.1	0.6	0.45	0.3
	1.8	0.2	0.7	0.4	1.4	1.5	0.6	1.9	1	0.1	1.9	0.1	1	0.6	0.3

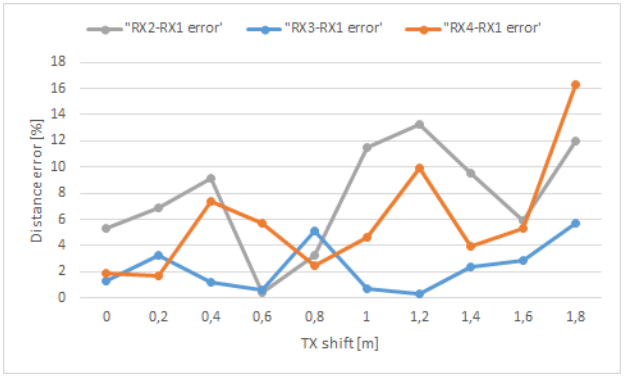

Fig. 18: Difference distance measurement error percentage

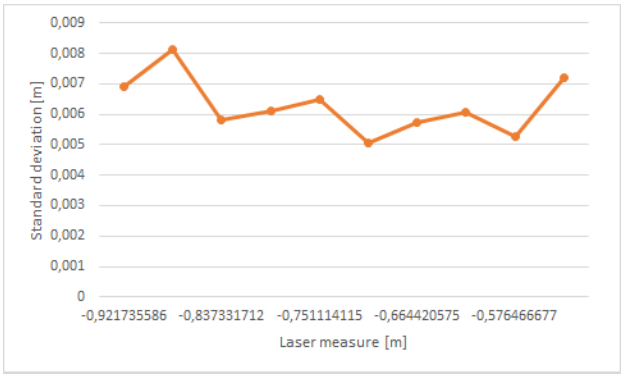

Fig. 19: Standard deviation of the measurements @ 100 MHz sampling rate

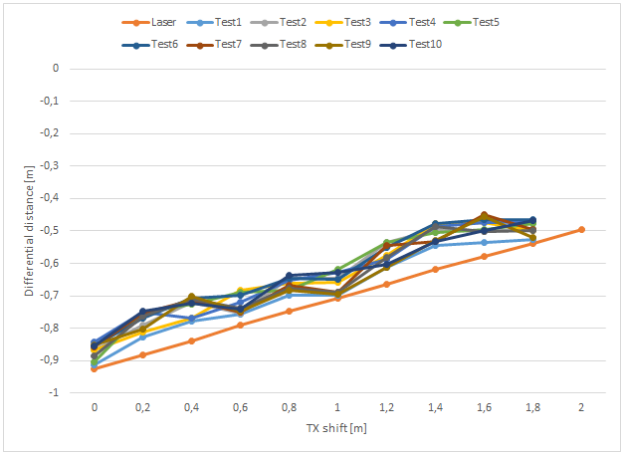

Fig. 20: RX2-RX1 differential measurements repeatability

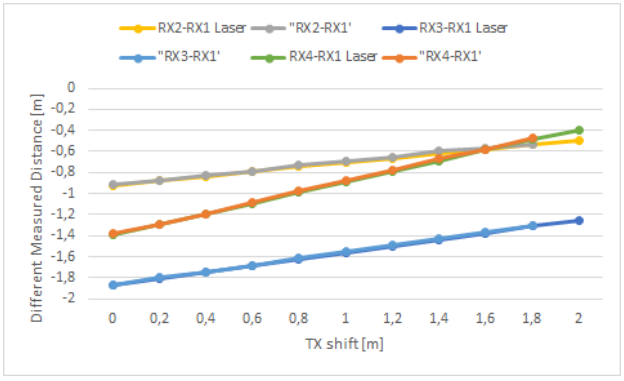

Fig. 21: Difference measured distance

solution is that it is highly scalable. In fact, the number of subcarriers can be easily changed addressing different regions of the LUT stored in the transmitter. The receiver evaluate the cross-correlation in equation (3) using a local copy of the transmitted signal. The numerical representation of the signal is computed off-line once and forever and the resulting samples are pre-loaded in memory, therefore not involving any on-line computation. The proposed system is not designed for a specific application and it can be used to extract the target position for both indoor and outdoor environments and may be adapted to 1D, 2D and 3D scenarios. Finally, the use of the FZC sequence leads to the further advantage that more than one transmitter can be localized by the system at the same time without introducing any interference between the signals, because their orthogonal properties depend on the chosen root index. In this case, the target position of the different transmitters are extracted using the reference copy of the sensing signal associated to the proper root index.

REFERENCES

[1] R. Macey and G. Ismail, "Wireless localization for mmwave networks in urban environments," *EURASIP Journal on Advances in Signal Processing*, vol. 2018, no. 1, 2018.

[2] M. Vossiek, L. Wiebking, P. Gulden, J. Wieghardt, C. Hoffmann, and P. Heide, "Wireless local positioning," *IEEE Microwave Magazine*, vol. 4, no. 4, pp. 77–86, Dec 2003.

[3] H. Liu, H. Darabi, P. Banerjee, and J. Liu, "Survey of wireless indoor positioning techniques and systems," *IEEE Transactions on Systems, Man, and Cybernetics, Part C (Applications and Reviews)*, vol. 37, no. 6, pp. 1067–1080, Nov 2007.

[4] F. Zafari, A. Gkelias, and K. K. Leung, "A survey of indoor localization systems and technologies," *IEEE Communications Surveys Tutorials*, vol. 21, no. 3, pp. 2568–2599, thirdquarter 2019.

[5] J. Koo and H. Cha, "Localizing wifi access points using signal strength," *IEEE Communications Letters*, vol. 15, no. 2, pp. 187–189, February 2011.

Fig. 22: Difference distance measurement error

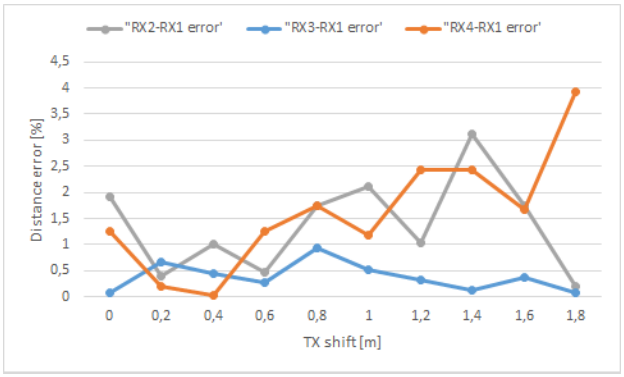

Fig. 23: Difference distance measurement error percentage

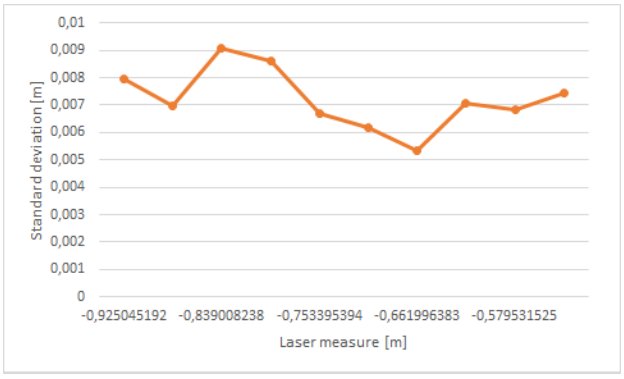

Fig. 24: Standard deviation of the measurements @ 250 MHz sampling rate

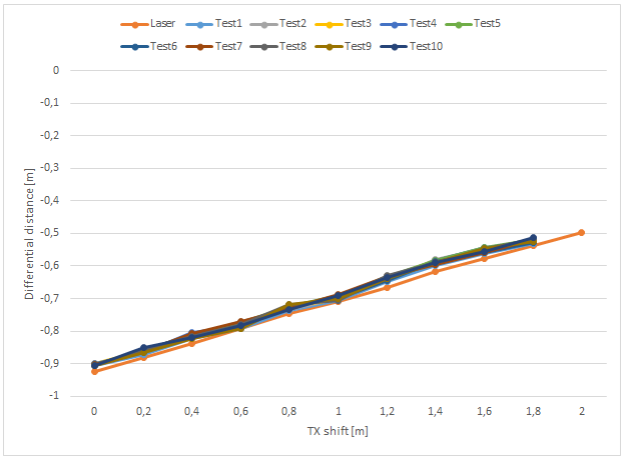

Fig. 25: RX2-RX1 differential measurements repeatability

[6] X. Wang, L. Gao, S. Mao, and S. Pandey, "Csi-based fingerprinting for indoor localization: A deep learning approach," *IEEE Transactions on Vehicular Technology*, vol. 66, no. 1, pp. 763–776, Jan 2017.

[7] R. C. Luo and T. J. Hsiao, "Dynamic wireless indoor localization incorporating with an autonomous mobile robot based on an adaptive signal model fingerprinting approach," *IEEE Transactions on Industrial Electronics*, vol. 66, no. 3, pp. 1940–1951, March 2019.

[8] N. A. A. Elhag, I. M. Osman, A. A. Yassin, and T. B. Ahmed, "Angle of arrival estimation in smart antenna using music method for wideband wireless communication," in *2013 International Conference on Computing, Electrical and Electronic Engineerinng (ICCEEE)*, Aug 2013, pp. 69–73.

[9] D. Inserra and A. M. Tonello, "A frequency-domain los angle-of-arrival estimation approach in multipath channels," *IEEE Transactions on Vehicular Technology*, vol. 62, no. 6, pp. 2812–2818, July 2013.

[10] R. Schmidt, "Multiple emitter location and signal parameter estimation," *IEEE Transactions on Antennas and Propagation*, vol. 34, no. 3, pp. 276–280, March 1986.

[11] A. Barabell, "Improving the resolution performance of eigenstructure-based direction-finding algorithms," in *ICASSP '83. IEEE International Conference on Acoustics, Speech, and Signal Processing*, vol. 8, April 1983, pp. 336–339.

[12] R. Roy and T. Kailath, "Esprit-estimation of signal parameters via rotational invariance techniques," *IEEE Transactions on Acoustics, Speech, and Signal Processing*, vol. 37, no. 7, pp. 984–995, July 1989.

[13] K. V. Rangarao and S. Venkatanarasimhan, "gold-music: A variation on music to accurately determine peaks of the spectrum," *IEEE Transactions on Antennas and Propagation*, vol. 61, no. 4, pp. 2263–2268, April 2013.

[14] G. Liu, H. Chen, X. Sun, and R. C. Qiu, "Modified music algorithm for doa estimation with nyström approximation," *IEEE Sensors Journal*, vol. 16, no. 12, pp. 4673–4674, June 2016.

[15] S. Ouelha, A. Aissa-El-Bey, and B. Boashash, "Improving doa estimation algorithms using high-resolution quadratic time-frequency distributions," *IEEE Transactions on Signal Processing*, vol. 65, no. 19, pp. 5179–5190, Oct 2017.

[16] Y. Wang, L. Wang, J. Xie, M. Trinkle, and B. W. . Ng, "Doa estimation under mutual coupling of uniform linear arrays using sparse reconstruction," *IEEE Wireless Communications Letters*, vol. 8, no. 4, pp. 1004–1007, Aug 2019.

[17] G. Piccinni, F. Torelli, and G. Avitabile, "Innovative doa estimation algorithm based on lyapunov theory," *IEEE Transactions on Circuits and Systems II: Express Briefs*, pp. 1–1, 2019.

[18] G. Han, D. Choi, and W. Lim, "A novel reference node selection algorithm based on trilateration for indoor sensor networks," in *7th IEEE International Conference on Computer and Information Technology (CIT 2007)*, Oct 2007, pp. 1003–1008.

[19] Y. Qi, C. B. Soh, E. Gunawan, K. Low, and A. Maskooki, "An accurate 3d uwb hyperbolic localization in indoor multipath environment using iterative taylor-series estimation," in *2013 IEEE 77th Vehicular Technology Conference (VTC Spring)*, June 2013, pp. 1–5.

[20] M. Vossiek, L. Wiebking, P. Gulden, J. Weighardt, and C. Hoffmann, "Wireless local positioning - concepts, solutions, applications," in *Radio and Wireless Conference, 2003. RAWCON '03. Proceedings*, Aug 2003, pp. 219–224.

[21] B. Jang and H. Kim, "Indoor positioning technologies without offline fingerprinting map: A survey," *IEEE Communications Surveys Tutorials*, vol. 21, no. 1, pp. 508–525, Firstquarter 2019.

[22] G. Wang, C. Gu, T. Inoue, and C. Li, "Hybrid fmcw-interferometry radar system in the 5.8 ghz ism band for indoor precise position and motion detection," in *2013 IEEE MTT-S International Microwave Symposium Digest (MTT)*, June 2013, pp. 1–4.

[23] B. Waldmann, R. Weigel, and P. Gulden, "Method for high precision local positioning radar using an ultra wideband technique," in *2008 IEEE MTT-S International Microwave Symposium Digest*, June 2008, pp. 117–120.

[24] M. R. Mahfouz, C. Zhang, B. C. Merkl, M. J. Kuhn, and A. E. Fathy, "Investigation of high-accuracy indoor 3-d positioning using uwb technology," *IEEE Transactions on Microwave Theory and Techniques*, vol. 56, no. 6, pp. 1316–1330, June 2008.

[25] M. Lipka, E. Sippel, and M. Vossiek, "An extended kalman filter for

TABLE III: Accuracy Comparison

Ref.	System Architecture	Frequency (GHz)	Reported Error	Bandwdth (MHz)
[24]	Carrier-Based UWB	5.4-10.6	3D 2-5mm	5000
[23]	Pulsed FMCW	7.5	1D 7mm	1000
[42]	Carrier-Based UWB	22.58-25.7	1D 0.1-2mm	3000
[43]	Impulse-Based UWB	2-7	1D 5-10mm	5000
[44]	Impulse-Based UWB	3.2-5.2	1D 1cm	3000
This Work	MultiCarrier WB	5.7-5.9	1D 2-8cm	40

direct, real-time, phase-based high precision indoor localization," *IEEE Access*, vol. 7, pp. 25 288–25 297, 2019.

[26] H. Xu, C. . Chong, I. Guvenc, F. Watanabe, and L. Yang, "High-resolution toa estimation with multi-band ofdm uwb signals," in *2008 IEEE International Conference on Communications*, May 2008, pp. 4191–4196.

[27] T. Ayhan, T. Redant, M. Verhelst, and W. Dehaene, "Towards a fast and hardware efficient sub-mm precision ranging system," in *2012 IEEE Workshop on Signal Processing Systems*, Oct 2012, pp. 203–208.

[28] K. Yu, K. Wen, Y. Li, S. Zhang, and K. Zhang, "A novel nlos mitigation algorithm for uwb localization in harsh indoor environments," *IEEE Transactions on Vehicular Technology*, vol. 68, no. 1, pp. 686–699, Jan 2019.

[29] R. Bharadwaj, S. Swaisaenyakorn, C. G. Parini, J. C. Batchelor, and A. Alomainy, "Impulse radio ultra-wideband communications for localization and tracking of human body and limbs movement for healthcare applications," *IEEE Transactions on Antennas and Propagation*, vol. 65, no. 12, pp. 7298–7309, Dec 2017.

[30] Y. Luo and C. L. Law, "Indoor positioning using uwb-ir signals in the presence of dense multipath with path overlapping," *IEEE Transactions on Wireless Communications*, vol. 11, no. 10, pp. 3734–3743, October 2012.

[31] F. Shang, B. Champagne, and I. N. Psaromiligkos, "A ml-based framework for joint toa/aoa estimation of uwb pulses in dense multipath environments," *IEEE Transactions on Wireless Communications*, vol. 13, no. 10, pp. 5305–5318, Oct 2014.

[32] G. Piccinni, G. Avitabile, and G. Coviello, "An improved technique based on zadoff-chu sequences for distance measurements," in *2016 IEEE Radio and Antenna Days of the Indian Ocean (RADIO)*, Oct 2016, pp. 1–2.

[33] ——, "A novel distance measurement technique for indoor positioning systems based on zadoff-chu sequences," in *2017 15th IEEE International New Circuits and Systems Conference (NEWCAS)*, June 2017, pp. 337–340.

[34] G. Piccinni, G. Avitabile, and G. Coviello, "Narrowband distance evaluation technique for indoor positioning systems based on zadoff-chu sequences," in *2017 IEEE 13th International Conference on Wireless and Mobile Computing, Networking and Communications (WiMob)*, Oct 2017, pp. 1–5.

[35] D. Chu, "Polyphase codes with good periodic correlation properties (corresp.)," *IEEE Transactions on Information Theory*, vol. 18, no. 4, pp. 531–532, July 1972.

[36] G. Piccinni, G. Avitabile, G. Coviello, and C. Talarico, "Modeling of a re-configurable indoor positioning system based on software defined radio architecture," in *2018 New Generation of CAS (NGCAS)*, Nov 2018, pp. 174–177.

[37] ——, "Analysis and modeling of a novel sdr-based high-precision positioning system," in *2018 15th International Conference on Synthesis, Modeling, Analysis and Simulation Methods and Applications to Circuit Design (SMACD)*, July 2018, pp. 13–16.

[38] Z. Sahinoglu, S. Gezici, and I. Gvenc, *Ultra-wideband Positioning Systems: Theoretical Limits, Ranging Algorithms, and Protocols*. New York, NY, USA: Cambridge University Press, 2011.

[39] Intel. (2018, June) Fft ip core, user guide. [Online]. Available: https://www.intel.com/content/dam/www/programmable/us/en/pdfs /literature/ug/ug_fft.pdf

[40] R. G. Lyons, *Understanding Digital Signal Processing*, 1st ed. Boston, MA, USA: Addison-Wesley Longman Publishing Co. Inc., 1996.

[41] G. Piccinni, G. Avitabile, G. Coviello, and C. Talarico, "Fpga-based implementation of a real-time distance evaluation algorithm for wireless localization systems," in *2019 IEEE Asia Pacific Conference on Circuits and Systems (APCCAS)*, Nov 2019, pp. 357–360.

[42] C. Meier, A. Terzis, and S. Lindenmeier, "A high precision wideband local positioning system at 24ghz," in *2006 IEEE MTT-S International Microwave Symposium Digest*, June 2006, pp. 1580–1583.

[43] G. Ossberger, T. Buchegger, E. Schimback, A. Stelzer, and R. Weigel, "Non-invasive respiratory movement detection and monitoring of hidden humans using ultra wideband pulse radar," in *2004 International Workshop on Ultra Wideband Systems Joint with Conference on Ultra Wideband Systems and Technologies. Joint UWBST IWUWBS 2004 (IEEE Cat. No.04EX812)*, May 2004, pp. 395–399.

[44] Z. N. Low, J. H. Cheong, C. L. Law, W. T. Ng, and Y. J. Lee, "Pulse detection algorithm for line-of-sight (los) uwb ranging applications," *IEEE Antennas and Wireless Propagation Letters*, vol. 4, pp. 63–67, 2005.